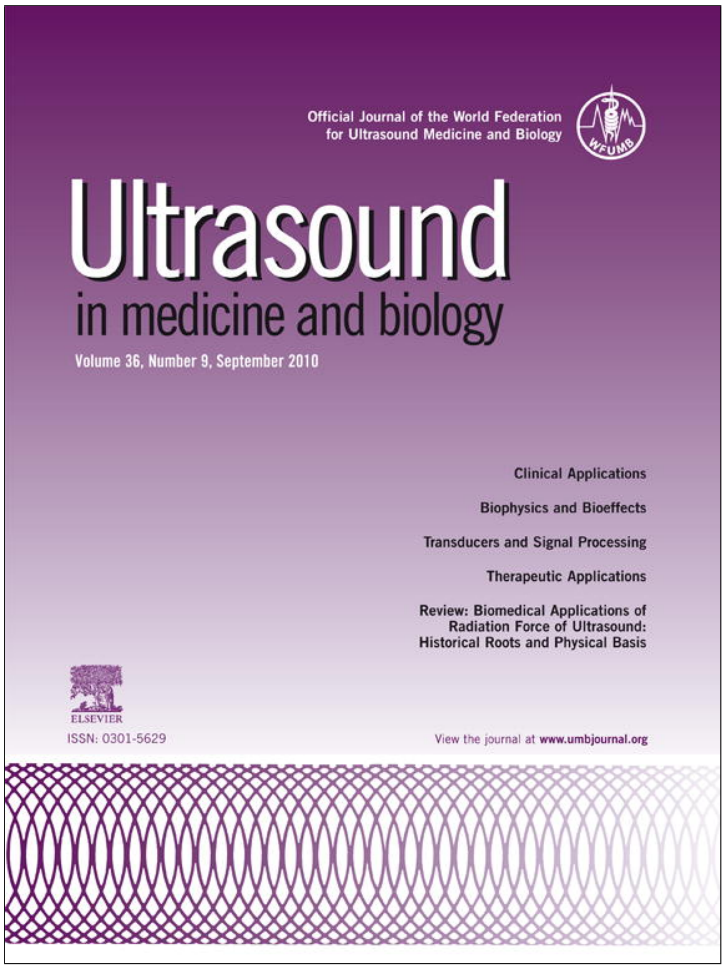

Ultrasound in Med. & Biol., Vol. 36, No. 9, pp. 1546–1558, 2010

0301-5629/$ - see front matter

ELSEVIER

doi:10.1016/j.ultrasmedbio.2010.05.025

● *Original Contribution*

AN INCREASE IN CELLULAR SIZE VARIANCE CONTRIBUTES TO THE INCREASE IN ULTRASOUND BACKSCATTER DURING CELL DEATH

Roxana M. Vlad,*† Ratan K. Saha,‡ Nehad M. Alajez,* Shawn Ranieri,§ Gregory J. Czarnota,*†¶ and Michael C. Kolios*‡

*Department of Medical Biophysics, Faculty of Medicine, University of Toronto; †Department of Radiation Oncology, Faculty of Medicine, University of Toronto; ‡Department of Physics, Ryerson University, Toronto, Ontario, Canada; §Department of Biomedical Engineering, University of Toronto, Toronto, Ontario, Canada; and ¶Imaging Research, Sunnybrook Health Sciences Centre, Toronto, Ontario, Canada

(*Received* 7 *January* 2009; *revised* 19 *May* 2010; *in final form* 25 *May* 2010)

Abstract—This study aims to explain the contribution of changes in cellular size variance (CSV) to increases in ultrasound-integrated backscatter (UIB) measured from cell samples undergoing cell death. A Monte Carlo algorithm was used to compare simulations of 2D distributions of cells, uniform (CSV = 0) *versus* heterogeneous (CSV > 0) and the same mean cellular size ($\overline{M}$). UIB increased in arrangements with heterogeneous cellular sizes from 3.6dB ($\overline{M}$ = 20 μm, CSV = 0 μm/CSV = 18 μm) to 5.6 dB ($\overline{M}$=10 μm, CSV = 0 μm/CSV = 8 μm). Experimentally, UIB (10 to 30 MHz) was measured from cell samples of four tumor cell lines viable and undergoing cell death after radiotherapy and chemotherapy treatment. An increase of 3.8–7.5 dB ($p < 0.001$) in UIB was measured from three cell lines. No increase in UIB was measured from one cell line. An increase in CSV was found for all cell samples after cell death. The results suggest that an increase in CSV could have a significant contribution to the increases measured in UIB after cell death in cell samples exposed to anticancer therapies. (E-mail: rvlad@lakeridgehealth.on.ca) **Crown Copyright © 2010 Published by Elsevier Inc. on behalf of World Federation for Ultrasound in Medicine & Biology.**

Key Words: **Ultrasound integrated backscatter, Cell death, Apoptosis and mitotic arrest, Anticancer therapies, Cellular size variance, Cellular sizes distribution, Simulation, Scatterer distribution, Monte Carlo algorithm.**

INTRODUCTION

Radiofrequency (RF) ultrasound data have been used extensively in medical ultrasound to analyze noninvasively the structural properties of different biological tissues. Quantitative ultrasound (QUS) methods based on the analysis of RF data have been used to diagnose prostate cancer, ocular tumors, liver and cardiac abnormalities (Feleppa et al. 1996, 2001; Insana et al. 1993; Lizzi et al. 1987, 1988, 1997a, 1997b, 1997c, 2003; Silverman et al. 2003; Yang et al. 2007), differentiate benign fibroadenomas from mammary carcinomas and sarcomas (Oelze et al. 2004; Oelze and O'Brien 2006; Oelze and Zachary 2006) and have provided good diagnostic accuracy in prostate cancer detection and lesion localization (Feleppa et al. 2004). One of the largely used QUS methods is the analysis of the RF backscatter spectrum. The RF spectrum can be related to the structure of a medium, if that medium can be modeled as a random distribution of scattering particles (Shung and Thieme 1993) and the characteristics of instrumentation are known. Under these conditions, it is well known that the frequency dependence of the RF spectrum is mainly dependent on the size of the dominant scattering structure in the medium, and the magnitude of the RF spectrum depends on the size, number density (number of scatterers per unit volume) and the relative acoustic impedance (fractional variation in acoustic impedance between the scattering particles and the surrounding medium) of the scattering particles.

Experimentally, ultrasound imaging and spectrum analysis techniques developed by Lizzi and co-workers (Lizzi et al. 1987, 1988, 1997a, 1997b, 1997c, 2003) were applied for the first time by Czarnota et al. (1997, 1999) and Kolios et al. (2002) to detect cell death in cell samples and tissues exposed to cancer therapies (*e.g.*, chemotherapy and photodynamic therapy). These studies indicated that apoptotic cells exhibited as much as a 16-fold increase in ultrasound backscatter intensity compared

Address correspondence to: Dr. Roxana M. Vlad, Department of Radiation Oncology and Medical Physics, University of Toronto, 1 Hospital Court, Oshawa, Ontario, O1G 2B9, Canada. E-mail: rvlad@lakeridgehealth.on.ca

with viable cells, as well as other measurable changes in ultrasound parameters, *i.e.*, changes in the spectral slope (Kolios et al. 2002; Vlad et al. 2008) and the backscatter intensity envelope statistics (Tunis et al. 2005). The same technique can be used to detect cell death by oncosis (Vlad et al. 2005) and mitotic arrest/catastrophe (Vlad et al. 2008). The applicability of ultrasound imaging and spectroscopy to detect noninvasive cell death has been demonstrated recently *in vivo* using different tumor types and cell death–inducing treatments (Banihashemi et al. 2008; Vlad et al. 2009).

The aim of cancer therapy is to kill tumors by inducing cell death (Tannock et al. 2005) that can be used as an indication of tumor response to cancer treatment. To date, methods for imaging cancer cell death in potential clinical settings are magnetic resonance methods based on measurements of the cytoplasmic-droplet accumulation that accompanies death in some cells, dynamic contrast-enhanced magnetic resonance imaging based on an increase in cellular membrane permeability in cells undergoing death, single photon emission computed tomography and positron emission tomography using radiolabeled annexin V (Brindle 2008). The use of these modalities to monitor anticancer therapy can be limited by their cost and the requirement of multiple injections of a contrast agent or radioactive substance. For this reason, these techniques have a reduced applicability in longitudinal preclinical and clinical studies.

The capability of ultrasound methods to detect changes in physical characteristics of tissue scatterers after cell death makes the technique promising as a method to monitor anticancer therapy in preclinical and clinical settings. Ultrasound is known to be a cost-effective imaging modality with widespread access worldwide. The advantage of this technique is that the process of cell death itself generates the contrast in ultrasound images as well as other significant changes in ultrasound parameters, allowing the assessment of the treatment effect and requiring no injection of exogenous contrast agents. To develop this ultrasound method for cancer therapy assessment, it is essential to understand which are the specific changes in cellular structure that are capable of generating this contrast in ultrasound images as well as changes of ultrasound parameters during the process of cell death.

Previous studies (Czarnota et al. 1997, 1999; Kolios et al. 2002; Taggart et al. 2007) have linked the changes in ultrasound images and spectral parameters to nuclear condensation and fragmentation after apoptotic cell death (*i.e.*, increase of scatterers' relative acoustic impedance and increase in number of scatterers per unit volume). However, ultrasound is also sensitive to other modalities of cell death, *e.g.*, oncotic cell death (Kolios et al. 2003; Vlad et al. 2005) and mitotic cell death (Vlad et al. 2008) characterized by increases in cellular and nuclear size, hence, contrasting with cellular changes that characterize apoptosis. Consequently, an interesting question is whether there are changes of cellular structure that commonly manifest in each of these modalities of cell death and that can be detected by ultrasound methods.

This study addresses this question by exploring a mechanism capable to explain how different modalities of cell death generate a contrast in ultrasound images and changes in ultrasound parameters. The changes in the magnitude and frequency dependence of backscattered ultrasound measured experimentally were linked to an increase in the cellular size variance (CSV) after cell death. To provide a framework to interpret the experimental observations, a Monte Carlo algorithm (Saha et al. 2008; Savery and Cloutier 2005) was used to simulate 2-D distributions of cells with uniform (CSV = 0) and heterogeneous cellular size (CSV > 0). Finally, the ultrasound parameters computed from simulations were compared with the ultrasound parameters measured from experiments.

Theoretical background

A Monte Carlo method, similar to that used previously to simulate ultrasound backscattering from distribution of nonaggregating red blood cells (Savery and Cloutier 2005; Saha et al. 2008), was applied here to simulate ultrasound backscattering by 2-D distributions of cells. Average frequency-dependent backscattering coefficient was computed from cell ensembles with uniform and heterogeneous sizes. The Metropolis algorithm (Metropolis et al. 1953) is an established method to investigate statistical properties of systems composed of many interacting particles and is capable of generating different system configurations. It has been considered suitable to characterize blood properties (Savery and Cloutier 2005; Saha et al. 2008). This algorithm was applied here to simulate different configurations of nonoverlapping cells accordingly to the Boltzmann probability distribution that was used to describe the probability distribution of energy states generated by the interactions between cells in the system. For instance, a certain energy state can characterize a particular spatial organization of cells and was obtained by summing various types of potentials (e.g., steric potential, electrostatic potential, adhesive potential, *etc.*) that dictate the interactions between cells.

The total energy of each configuration of the system was computed by summing the pair interaction energies between the particles in the system. The probability distribution of energy states, where each energy state (E) can correspond to one or more than one configuration is given by the Boltzman distribution:

$$p(E) = \frac{1}{Z}\exp\left(-\frac{E}{k_B T}\right) \quad (1)$$

where k_B, T and Z are the Boltzmann constant, absolute temperature and the partition function of the system, respectively. Equation (1) indicates that lower-energy states are more probable than higher-energy sates; consequently, lower-energy states contribute more to the bulk properties of the system. Therefore, the ensemble average of a quantity of interest that characterizes the system can be estimated by taking its weighted sum over those lower states. In this method, each new configuration of the system was generated according to its Boltzmann probability by using the Metropolis algorithm to establish the equilibrium states. When a new particle throw was introduced, the Metropolis algorithm (Metropolis et al. 1953) was used to accept or reject that throw, where particle represents a scatterer and throw is a move to assign spatial coordinates to the scatterer. This corresponded to one Metropolis step. Using this algorithm, the energy states with higher probabilities were generated more frequently. This ensured that ensemble average values estimated for each of the 2D particle configurations approached a realistic value.

The cells were allowed to occupy random positions within the region-of-interest (ROI). Interaction energy of each particle was determined as a function of its neighbor coordinates under periodic boundary conditions. These conditions dictated the placement of the particles along the x and y directions in a 2-D sample and were imposed in this study to remove the edge effects. Briefly, the periodic boundary conditions allowed the particles at the right edge to interact with those at the left edge and the particles at the top edge of the sample to interact with those at the bottom edge.

The method considered the particular case of spherical nonoverlapping cells. The cells do not overlap if their center-to-center separation distance is larger or equal with the sum of each cell radius. First, a configuration was generated by throwing all the particles randomly in the ROI. For this configuration, the pair potential energy was set to $10^6 k_B T$ for each overlapping pair and 0 for a nonoverlapping pair. The total energy was computed, and then the system was allowed to evolve by introducing random moves to randomly selected particles. The Metropolis algorithm was used to determine whether each move is accepted or rejected. The procedure generated minimal energy states in which the interaction energy of each two particles was zero. Consequently, the total energy of the system, in terms of interaction energy, was zero. Then, the frequency-dependent backscattering coefficient and differential backscattering cross section were computed from these cell arrangements over a large number of realizations to obtain their ensemble average.

Acoustical waves propagating in a biological sample are scattered when these encounter density and speed-of-sound inhomogeneities. In the context of acoustic, cell samples can be roughly described as dense collections of rigid spherical particles that are randomly packed to occupy a certain volume. Cells can be considered weak scatterers because they have to be closer than their own diameter for their scattered pressure to be significantly affected by multiple scattering (Chin et al. 2001). Because the multiple scattering can be neglected, the scattered field in the backscattering direction at a large distance r from the center of the ROI comprising a collection of nonoverlapping, randomly positioned cells can be obtained by linear superposition of scattered signals by each cell. The analytical expression of the backscattering coefficient valid for the entire frequency range can be written from Twersky (1978) as:

$$\chi_b = m\left\langle \frac{1}{N}\left|\sum_{q=1}^{N} e^{i2\vec{k}\cdot\vec{r_q}}\Phi_{bq}(k,a_q)\right|^2\right\rangle \qquad (2)$$

where m is the number density of particles, N is the number of scatterers in the ROI, $\vec{k}$ is the incident acoustic wave vector, Φ_{bq} is the exact analytical solution of backscattering amplitude (Morse and Ingard, 1968) for the q^{th} spherical scatterer that was considered as a fluid sphere with radius a_q and position vector r_q. This equation was computed for each cell distribution with uniform and heterogeneous sizes to determine frequency-dependent backscattering coefficients. Similar expression has been used to describe the backscattering coefficient of red blood cells (Savery and Cloutier 2005; Shung and Thieme 1993; Saha et al. 2008). In that context and for cells with uniform size, the backscattering amplitude is constant for all cells and can therefore be factored out from the summation. Also, the expression of the backscattering coefficient for particles with equal radii can be written in a simplified form (Savery and Cloutier 2005; Shung and Thieme 1993):

$$x_b = mW|\Phi_b(k,a)|^2, \qquad (3)$$

where W is the Percus-Yevick packing factor for hard disks in two dimensions, which is described in eqn (4):

$$W = \frac{(1-H)^3}{1+H} \qquad (4)$$

and H is the packing fraction. The backscattering coefficient predicted by eqn (3) was computed and compared with that of eqn (2) to validate the computer code developed for the implementation of eqn (2). It is of interest to notice that the backscattering amplitude is different for different scatterer sizes and cannot be factored for ensembles of cells with heterogeneous size.

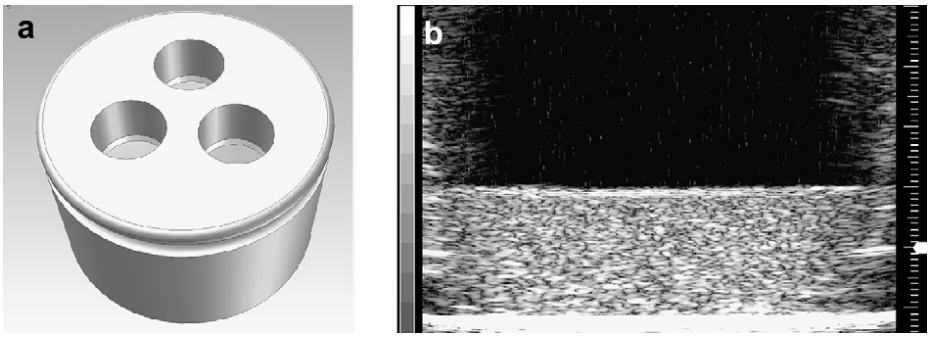

Fig. 1. (a) Image of the sample holder. The sample holder was made of stainless steel and had two parts: a flat bottom, very-fine polished to have an ultrasound signal reflection comparable with the transmitted signal, and a stainless steel disk with three cylindrical holes cut through it (8 × 7 mm; diameter × height). The flat bottom was attached with screws to the stainless steel disk and the bottom of the wells were cushioned with Teflon rings. Teflon rings ensured that the content of the wells was not spilled between compartments during the sample centrifugation. Two samples can be prepared once by centrifugation in two wells. The other well serves as a calibration reference. (b) Ultrasound image of a compact aggregate of cells in the sample holder. The height of the cell sample is ~2 mm, the smallest division on the scale on the lateral side of cell samples is 0.1 mm. The small triangle on the right side of each cell sample represents the location of the transducer focal point. The hyperechoic lines across the bottom, right and left side of the ultrasound image are the bottom and the walls, respectively, of the sample holder.

METHODS

Cell preparation

Acute myeloid leukemia cells (OCI-AML-5) (Wang et al. 1991) were grown from frozen stock samples as described elsewhere (Taggart et al. 2007). FaDu and Hep-2 cell lines were obtained from the American Type Culture Collection (ATCC, Manassas, VA, USA). C666-1 cells (Cheung et al. 1999; Li et al. 2002) were maintained in RPMI 1640 cell culture media (Invitrogen Canada Inc., Burlington, ON, Canada) supplemented with 10% fetal bovine serum (FBS) (Cansera International Inc., Etobicoke, ON, Canada) and antibiotics (100 mg/L penicillin and 100 mg/L streptomycin) (Bioshop, Burlington, ON, Canada). FaDu cells were cultured in Eagle's minimum essential media (Invitrogen Canada Inc.) with 2 mM L-glutamine and Earle's balanced salt solution adjusted to contain 1.5 g/L sodium bicarbonate, 1.0 mM sodium pyruvate (Sigma-Aldrich Co., Oakville, ON, Canada) and 10% FBS. Hep-2 cells were cultured in minimum essential media supplemented with 10% FBS and 0.1% gentamycin (Hoffman-La Roche Ltd., Mississauga, ON, Canada). All cell lines were grown in a humidified atmosphere at 37 °C, containing 5% CO_2.

All cell lines were exposed to radiotherapy. The AML cell line was also exposed to chemotherapy. It was expected that radiotherapy and chemotherapy would result in different forms of cell death in these cell lines (Czarnota et al. 1999; Kolios et al. 2002; Vlad et al. 2008). Cells were irradiated using a small animal and cell irradiator, the Faxitron Cabinet X-ray System (Faxitron X-ray Corporation, Wheeling, IL, USA) that delivered 160-keV X-rays at a rate of 200 cGy/min. The cells from AML cell line were treated separately with the chemotherapeutic drug cis-platinum (cisplatin) at 10 μg/mL that induced apoptosis in this cell line (Czarnota et al. 1999; Kolios et al. 2002; Tunis et al. 2005). Cells were treated with the drug for 0, 12, 24, 48 and 72 h.

The cell cultures were examined daily under light microscopy to confirm cell death. Structural changes that are characteristic of apoptotic or mitotic response (*i.e.*, increase in cell and nuclei size, membrane ruffling, cytoplasm vacuolization, nuclear fragmentation and condensation and formation of apoptotic and mitotic bodies) were used as an indication of cell death (Darzynkiewicz et al. 2001). These structural changes were observed in AML cell culture for all time points of treatment with cisplatin and at all applied radiotherapy doses. For the head and neck cancer cell lines, most of these changes were observed with the 8-Gy radiation dose at 48 h after exposure to radiotherapy.

Before ultrasound data acquisition, cells were trypsinized (Hep-2, FaDu and C666-1) and washed in phosphate-buffered saline (PBS). AML cells grew in suspension and did not need to be trypsinized. After washing in PBS, cells were centrifuged at 1900 g to form compact aggregates of cells, referred to in this study as *cell samples*. These cell samples likely emulate the spatial distribution and packing of cells in tumors (Vlad 2009). Treated and viable samples were prepared by centrifugation of cells in two separate wells of a custom-built sample holder (Fig. 1a). The cell samples were independently prepared in triplicate from different sets of cells. A representative ultrasound image of a compact aggregate of cells (cell sample) in the sample holder is presented in Fig. 1b.

Ultrasound data acquisition and analysis

A VS40B high-frequency ultrasound device (VisualSonics Inc., Toronto, ON, Canada) was used to image the cell samples. A focused transducer with a nominal center frequency of 20 MHz (20 mm focal length, 10 mm aperture diameter, –6 dB bandwidth of 11 to 28 MHz) was used to collect ultrasound data. Data were collected within the transducer depth of field (3.12 mm calculated at the transducer nominal frequency), from five different planes containing 40–60 8-bit RF lines sampled at 500 MHz. The ROIs chosen to calculate the backscattered power spectra contained 15–25 independent scan lines each, at a distance of 250 μm (the transducer beamwidth at the nominal center frequency) and were 1 mm deep and centered around the transducer focus.

Ultrasound scan lines from each bracketed line segment were multiplied by a Hamming weighting function to suppress spectral lobes, and the Fourier transform was computed. The squared magnitudes of the resultant spectra from all ROIs were averaged and divided by the power spectrum computed from a flat quartz calibration target to calculate the normalized power spectra. This procedure removed system and transducer transfer functions to provide a common reference for data collected with various transducers and systems (Lizzi et al. 1997). The normalized power spectra measured from each sample were compensated for frequency-dependent attenuation losses according to Taggart et al. (2007) using the attenuation coefficients reported recently in a recent publication (Vlad et al. 2008) for AML, FaDu and Hep-2 cell samples, viable and treated with radiotherapy. The rest of the attenuation coefficients for AML and C666-1 cell samples, viable and exposed to chemotherapy and radiotherapy, respectively, are presented in Table 1. These attenuation coefficients were calculated as a function of frequency using a broadband technique (Bamber 1997). To calculate the UIB, the resulting normalized power spectra were integrated over the transducer –6 dB bandwidth. Linear regression analysis was used to calculate the spectral slope (SS) from the normalized backscatter power. The SS is an indicator of effective scatterer size, and a decrease in SS corresponds to an increase in effective scatterer size when properly corrected for attenuation according to Lizzi and colleagues (Lizzi et al. 1997a, 1997b 1997c, 2003).

Cytology analysis and measurements of cellular and nuclear size

After the acquisition of ultrasound data, the cell samples were fixed in 10% buffered formalin (Fisher Scientific, Neapan, ON, Canada) for a minimum of two days. The fixed cell samples were carefully removed from the sample holder and embedded in agar gel to preserve the shape and integrity of the sample. The agar-embedded cell samples were subsequently sectioned and placed in a cassette for paraffin embedding so that the microtome sections were taken from the same plane as the ultrasound data. The sections were stained with hematoxylin and eosin (H&E).

Table 1. Attenuation coefficients for AML cell samples treated with chemotherapy and C666-1 cell samples, viable and treated with radiotherapy

Cell type	ATS ± SE (dB/mm/MHz)
C666-1 control	0.065 ± 0.011
C666-1 8 Gy	0.070 ± 0.014
AML 12 h	0.058 ± 0.012
AML 24 h	0.062 ± 0.010
AML 48 h	0.070 ± 0.009
AML 72 h	0.130 ± 0.015

Three cell samples were considered for each experimental condition and SE represents the standard errors. These values were used to correct the ultrasound backscatter and spectral slopes for attenuation.

Cell and cellular fragment sizes for each experimental condition were measured with a Multisizer3 Coulter Counter (Beckman Coulter, Mississauga, ON, Canada) using a 100-μm aperture that allowed precise and reliable measurements of particle size. This method allowed precise measurements of 5000–10,000 cells per treatment condition within the range of 5–60 μm.

Flow cytometric analysis using propidium iodine (Invitrogen Canada Inc., Burlington, ON, Canada) was performed to measure cell DNA content (Pozarowski et al. 2003). Cells were harvested, washed twice in fluorescent activated cell sorting (FACS) buffer (PBS/0.5% bovine serum albumin), resuspended in 1 mL of FACS buffer and fixed for 1 h on ice in 3 mL of ice-cold 70% ethanol. Cells were washed once before being resuspended in 500 μL of FACS buffer supplemented with 40 μg/mL RNAse A (Sigma-Aldrich Co., Oakville, ON, Canada) and 50 μg/mL propidium iodine; then cells were incubated at room temperature for 30 min in the dark before being analyzed in a FACS Caliber (BD Biosciences, Mississauga, ON, Canada) using FL-2A and FL-2W channels. The results are presented as the percentage number of cells found in different phases of the cell cycle. This classification is dependent on DNA content and helps to identify the forms of cell death after each of the applied therapies. The sub-G_1 fractions were identified as apoptotic cells because the nucleus becomes fragmented during apoptosis. The sub-G_1 peak can represent, in addition to apoptotic cells, mechanically damaged cells and cell fragments in advanced stages of cell death (Darzynkiewicz et al. 1997, 2001). The G_1 peak represents phenotypic normal cells. The G_2/M peak is identified as cells in mitosis and mitotic arrest, whereas the peak with higher than double DNA content (higher than the G_2/M fraction) was identified as cells in mitotic

catastrophe and polyploid cells. Cells typically die by mitotic arrest/catastrophe after they undergo as many as four unsuccessful mitotic cycles as described by Tannock *et al.* (2005), and they are characterized by enlarged cells and nuclei.

Simulation

The size of the area to be investigated was fixed to 500 × 500 μm. This area was assumed to be filled 100% by cells of a specific average cellular size that matched the average cellular size measured experimentally. This ensured a constant number of cells of a particular size per sample. The nuclei were placed randomly within the ROI, one nucleus per cell. The nuclei embedded in cytoplasm were treated as scatterers for the incident ultrasound waves because their acoustic properties were different with respect to the cytoplasm. It was considered that nuclei covered 50% of the cell area, irrespective of its size. This value was chosen because it has been reported that the maximum possible packing in 2-D for random loose packed configurations of disks with equal radii is between 52% and 55% (Hinrichsen et al. 1990). This value is within the range of the values calculated from the cell lines used in these experiments for the nucleus-to-cell area ratio (between 49%–68%). Furthermore, a packing of 50% of nuclei ensured a reasonable allocation of computing time. Typically, the computational time varies exponentially with the number of particles, which is determined by the size of the ROI and particle packing. For example, the execution time for a simulation of particle distribution with a diameter of 15 μm was nearly 2 h on a remote computer cluster. The execution time for the simulation of another sample, which contained more particles with a diameter of 8 μm, took approximately 8 h on the same computing platform. The quantities of interest (frequency-dependent backscattering coefficient and differential backscattering cross section) were computed over a large number of configurations and their ensemble averages were determined. For instance, for a cell sample containing particles with a diameter of 10 μm, 800,000 iterations were sufficient to obtain converging results for each simulation and for a 10 ± 8-μm sample, 250,000 Metropolis steps were used. For each sample, the number of iterations was sufficiently large so that the average parameters that characterize the ensemble did not vary significantly with the number of iterations. This procedure was repeated 25 times for each set of parameters, and average values of those quantities were obtained.

At least two cases were considered for each average particle size, *e.g.*, uniform distributions in which all particles have the same size (CSV = 0) and heterogeneous distributions in which particles have different sizes (CSV >0) and followed a Gaussian distribution. It has been assumed that the area covered by particles remained constant from uniform to heterogeneous particle size. For symmetric distributions around the mean, a large variance—larger than the average particle diameter—can result in a negative diameter that is unphysical. Consequently, the maximum variance allowed by the simulation was chosen that the diameter of the smallest particles remained 2–3 μm. The frequency-dependent backscattering coefficients from particle simulations were computed using eqn (2) and compared with the Percus-Yevick packing theory to validate the computer code (Fig. 2c).

The density and sound velocity within the scatterer were chosen as ρ_e = 1180 kg/m^3 and c_e = 1523 m/s, respectively. Corresponding quantities of the surrounding medium were taken as ρ_0=1000 kg/m^3 and c_0 = 1483 m/s, respectively. These values were chosen because the Anderson model with this set of values fitted well the backscattering intensity pattern for PC-3 cells, with a value of the nucleus-to-cell area ratio of approximately 50% (Baddour and Kolios, 2007). Since this value of nucleus-to-cell area ratio is within the range of values of nucleus-to-cell area ratio measured from the cell lines used in this study, it was used in the simulations and it was considered that these values for density and speed of sound approximated well the density and speed-of-sound properties of the cell lines used in this study.

RESULTS

In the first part of this section, results from simulation of 2-D distributions of particles with uniform and heterogeneous sizes, respectively, are presented. In the second part, measurement of ultrasound parameters, qualitative histological observations, quantitative analysis of cell death and measurement of cellular sizes are presented.

Simulation

Representative diagrams illustrating 2-D distributions of nuclei with uniform and heterogeneous sizes are shown in Fig. 2 (a, b). The nuclei corresponding to cells with uniform size of 10 μm and heterogeneous size of 10 ± 8 μm, respectively, were randomly positioned in a rectangular area restricted to a nonoverlapping condition. In Fig. 2(c), frequency-dependent backscattering coefficients corresponding to these particle arrangements are plotted. The backscattering coefficient predicted by the Percus-Yevick packing theory is also plotted, for comparison, on the same graph. The backscattering coefficient curve computed from the uniform particle size distribution was in good agreement with the Percus-Yevick packing theory within a frequency regime for which $ka << 1$, where $k = 2\pi/\lambda$, λ is the wavelength and a is the particle radius. Because the Percus-Yevick packing theory is valid in the lower-frequency range, the

Percus-Yevick curve did not match well with the curve simulated for monodisperse cells for frequencies larger than 30 MHz (*i.e.*, $ka > 0.44$). Within the same frequency range ($ka << 1$), the backscattering coefficient increased for the heterogeneous particle size distributions because of larger particles in the distribution of sizes (Fig. 2c). Within this frequency range, the particles behaved more like Rayleigh scatterers, with an increase of the backscattering cross-section with the fourth power of frequency. For $ka \leq 1$, the difference between the backscattering coefficient curves, computed from simulation of uniform and heterogeneous particle distributions, diminished until they became equal, then slightly reversed for $ka > 1$. For heterogeneous particle distributions, the positions of the maxima and minima were different for different cellular sizes, resulting in a smoother variation of the backscattering coefficient at these higher frequencies. For instance, at higher frequencies the oscillatory pattern predicted by the Percus-Yevick packing theory diminished for the cellular distribution with smaller CSV (10 ± 2 μm) and reduced to an approximately flat curve for the distribution with largest CSV (10 ± 8 μm).

The UIB computed from simulation of particle distribution with uniform and heterogeneous sizes over a frequency range of 10–30 MHz is shown in Fig. 3. As expected, the UIB increased from –58.4 to –45.0 dB, with an increase of particle size from 10 to 20 μm, for uniform particle size distributions. The increase in the variance of particle size resulted in significant differences ($p < 0.001$) between UIB measured from distribution with uniform and heterogeneous sizes for the same average particle size. The increase to the maximum variance of particle size had a stronger influence over the increase in UIB for particles with smaller sizes, *e.g.*, 10–15 μm. For example, the UIB difference between the distribution with uniform particle size and heterogeneous particle

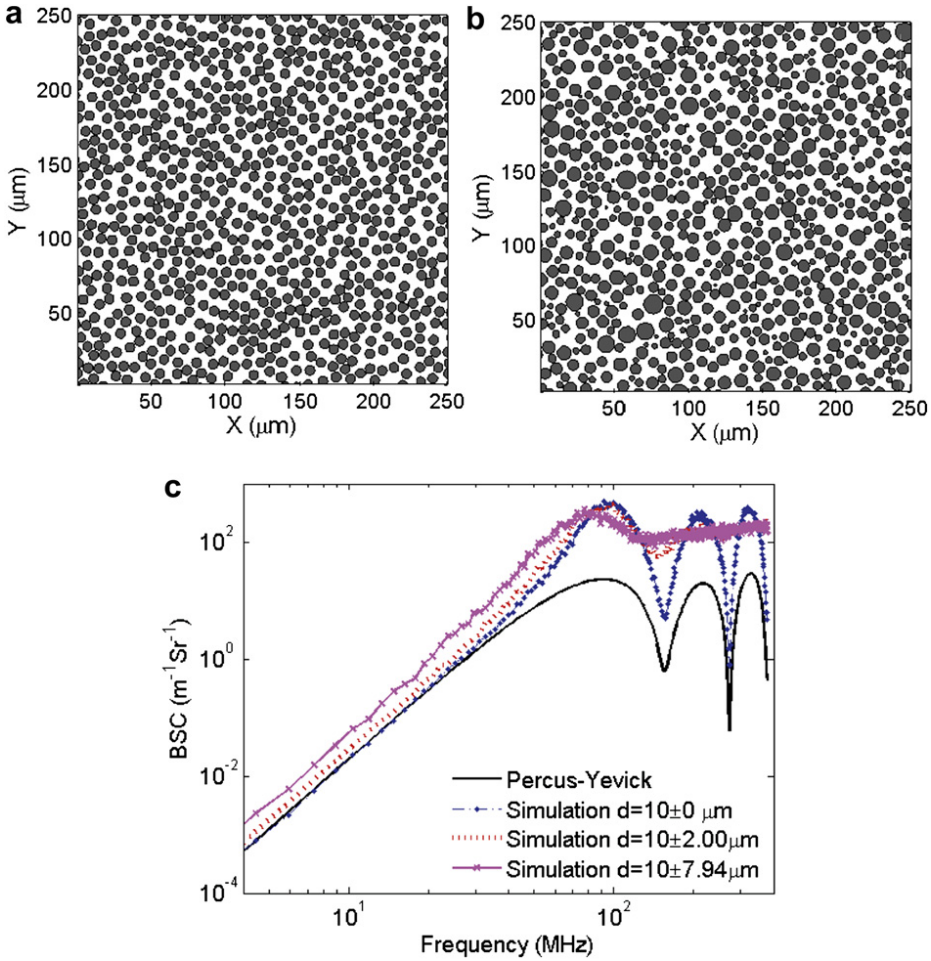

Fig. 2. Spatial arrangements of nuclei corresponding to the cells with uniform sizes (a) and heterogeneous sizes (b) distributed over an area of 250 × 250 μm^2. For clarity, spatial arrangements within 250 × 250 μm are presented; however, the backscattering coefficient was computed for 500 × 500-μm sample size. (c) Plots of frequency-dependent backscattering coefficients corresponding to the arrangement from (a) and (b) and the plot of backscattering coefficient predicted by the Percus-Yevick packing theory for cells with uniform size.

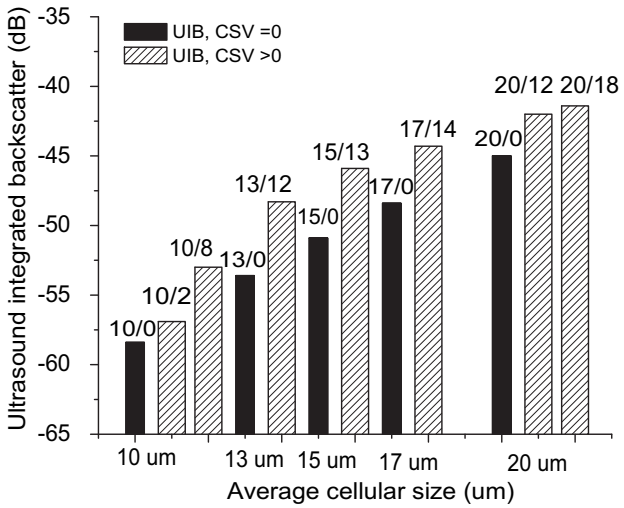

Fig. 3. Plot of UIB values computed from simulations of particle distributions with uniform and heterogeneous sizes from 10 to 20 μm. The labels at the top of each column-bar represent the average and variance of cellular size.

size decreased as the average particle size and CSV increased from 5.3 dB for 10 μm (CSV $\sim$8 μm) to 3.5 dB for 20 μm (CSV $\sim$17.5) μm, as represented in Fig. 3. The maximum variance of particle size was considered ($\sim(\overline{M}-2)\mu$m) where 2 μm represents the minimum scatterer size allowed by the simulation.

Experimental data

The plot of UIB changes measured from the AML cell samples exposed to chemotherapy and radiotherapy as a function of the duration of the exposure to the drug and the radiation dose is plotted in Fig. 4(a). The UIB increased by 4.5 to 7.5 dB ($p < 0.001$), with a maximum increase after 48-h exposure to the drug for AML cell lines exposed to chemotherapy, and the UIB increased by 3.8 to 7.1 ($p < 0.001$), with a maximum increase at 4-Gy radiation dose for AML cell sample exposed to radiotherapy.

Histology of AML cell samples control and exposed to chemotherapy and radiotherapy are shown in Fig. 4(b). The histology indicated that the control cell sample had a uniform cell composition with cells of approximately similar sizes, whereas cell samples exposed to cancer therapies underwent distinct structural changes after cell death. For instance, the histology of AML cells exposed to cisplatin presented the characteristics of cell death by apoptosis characterized by nuclei condensation and fragmentation, with a general appearance of smaller cellular size. In contrast, the histology of AML cells exposed to radiotherapy exhibited a mix of cell death, apoptosis and mitotic arrest characterized by enlarged cells and nuclei (Tannock et al. 2005), with a general appearance of larger cellular size.

To confirm and quantify different forms of cell death, measurements of DNA content in cell sample were conducted, in addition to histology (Fig. 4c). Analysis of DNA content in AML cells treated with chemotherapy indicated gradual increases in the apoptotic fractions (from 0.3% at 0 h to 6.9% at 12 h, 30.8% at 24 h, 42.4% at 48 h and 55.4% at 72 h) depending on the duration of the exposure to the drug. No significant increases in mitotic fractions (G_2/M) were measured at any of these time points (Fig. 4c). Analysis of DNA content in AML cells treated with radiotherapy revealed a mix of cell death, apoptosis and mitotic catastrophe, with increases in the apoptotic fractions (from 0.6% at 0 Gy to 6.2% at 2 Gy, 9.2% at 4 Gy, 8.1% at 8 Gy) and mitotic arrested fractions (from 10.7% at 0 Gy to 27.0% at 2 Gy, 36.4% at 4 Gy, 36.5% at 8 Gy).

To determine how the sequence of cell death affected cellular size and the distribution of cellular size, precise measurements of cellular size distributions were conducted using a Multisizer 3 Coulter Counter (Beckman Coulter). Cellular size distributions of AML cell samples before and after exposure to the therapy are presented in Fig. 5. After cell death, there was an increase in the number of either smaller particles (consistent with apoptosis) in cell samples exposed to chemotherapy or both smaller and larger particles (consistent with the mix of mitotic arrest and apoptosis) in cell samples exposed to radiotherapy. UIB values and corresponding measurements of cellular sizes for all experimental conditions studied for AML cells are presented in Table 2.

The experimental data corresponding to the rest of the cell lines FaDu, Hep2 and C666-1, *i.e.*, the UIB values, average and variance of cellular size, relevant fraction resultant from the measurements of DNA content before and after radiotherapy, are presented in Table 3. The UlB increased in FaDu and Hep2 cell samples and did not increase in C666-1 cell samples after exposure to radiotherapy (Table 3). The cell samples from these cell lines (FaDu, Hep2 and C666-1) died predominantly by mitotic arrest/catastrophe because no apoptotic (sub-G_1) fractions were detectable and the mitotic arrested cell fraction and polyploidy cell fraction increased after the treatment with 8-Gy radiation dose (Table 3). The average and variance of cellular size increased, consistent with the predominant modality of cell death, mitotic arrest/catastrophe exhibited by these cell lines after radiotherapy (Table 3). The CSV in control and treated C666-1 cell samples was very large: CSV= 26.0 μm ($\overline{M}$=13.0 μm) and CSV=33.3 μm ($\overline{M}$=14.7 μm), respectively, with cellular size reaching well beyond 20 μm, as shown in Fig. 5c. The simulation results indicated that within the frequency range of 10–30 MHz, ultrasound backscattering is less sensitive to changes in cellular size for large sizes, *e.g.*, $\geq$20 μm (Fig. 3). Therefore, no increase in UIB was

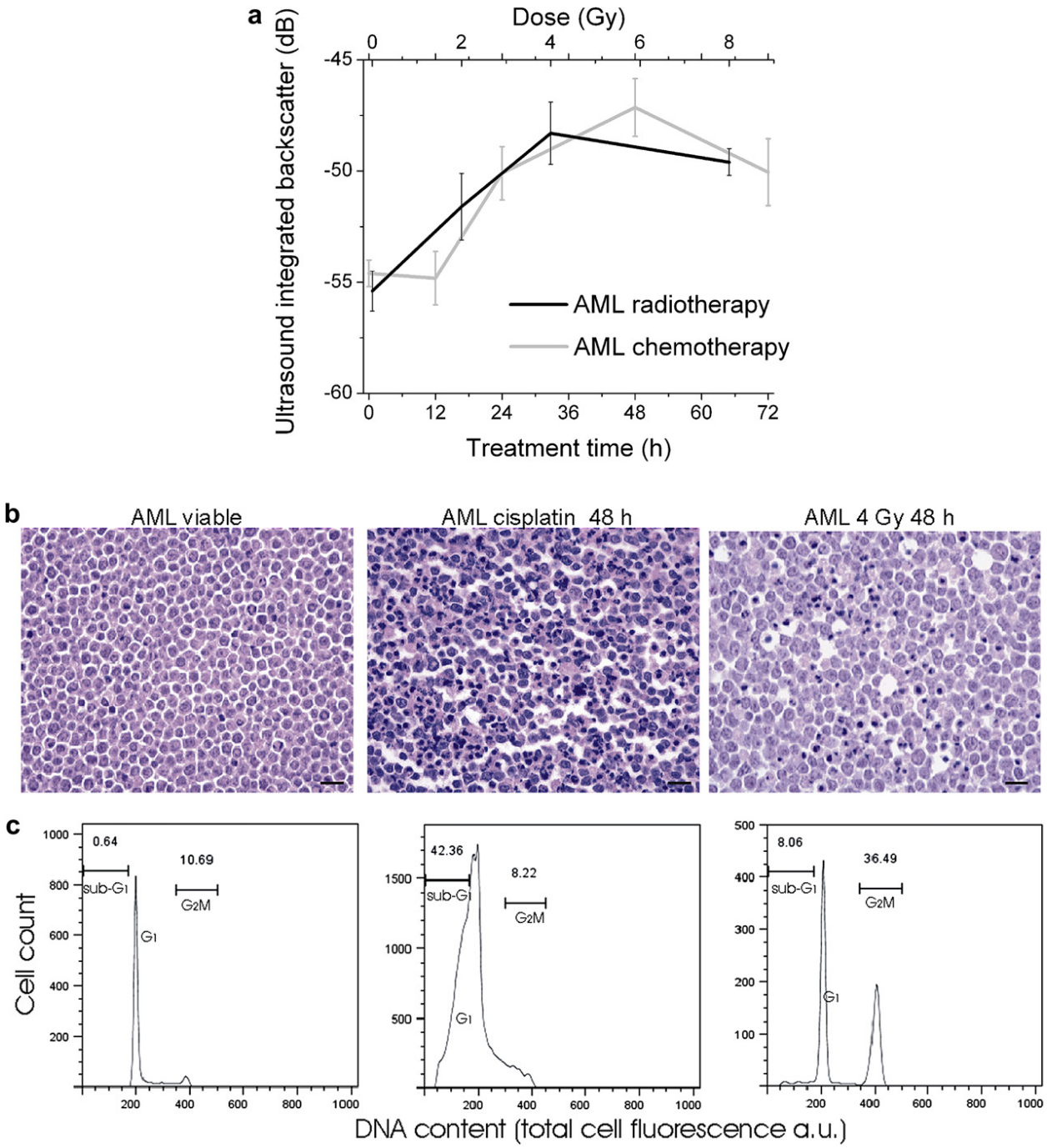

Fig. 4. The UIB of AML cell samples exposed to cisplatin and radiotherapy, representative H&E staining and corresponding measurements of DNA content of AML cell samples corresponding to the maximum increase in UIB. The ultrasound data were collected at 48 h after the cell samples were exposed to radiotherapy. (a) The UIB increased for AML cell lines exposed to chemotherapy by 4.5 to 7.5 dB, with a maximum increase after 48-h exposure to the drug. The UIB increased for AML cell sample exposed to radiotherapy by 3.8 to 7.1, with a maximum increase at 4-Gy radiation dose. (b) H&E images of AML-viable samples, illustrating the normal phenotype of these cell lines, AML cell samples exposed to cisplatin for 48 h and AML cell samples exposed to 4-Gy radiotherapy. The white spaces in the staining represent histological artifacts caused by cell cytoplasm retraction with fixation procedure. These artifacts are typically more pronounced in the tissue regions presenting advanced cell death. (c) Quantitative measurement of cell death corresponding to the histology from the upper panel demonstrating increase in apoptotic fractions with no significant change in mitotic arrested cell fractions for AML cell samples treated with cisplatin, and increases in both apoptotic and mitotic-arrested cell fractions for cell samples treated with radiotherapy.

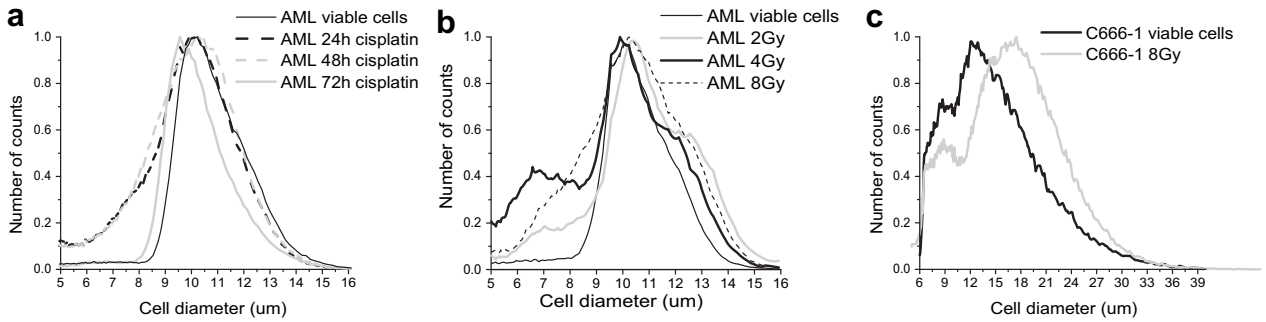

Fig. 5. Histograms of cell size distributions. (a) AML cells treated with cisplatin for different periods of time, (b) AML cells treated with different doses of radiotherapy and counted at 48 h after exposure and (c) C666-1 cells treated with radiotherapy. The histograms are normalized to one by dividing each count from the distribution to the maximum count.

measured for C666-1 cell samples after radiotherapy, although they exhibited the characteristics of cell death similar to the other two cell lines (FaDu and Hep-2).

SS is an indicator of effective scatterer size and a decrease in SS corresponds to an increase in effective scatterer size when properly corrected for attenuation (Lizzi et al. 2003). Values of SS computed from AML cell samples exposed to radiotherapy and chemotherapy, Hep-2 and FaDu cell samples exposed to radiotherapy, and the correlation of these results with measurements of cellular size, have been published previously. For completeness, a summary of these results is presented here. The SS calculated for AML cell samples did not change significantly between the samples treated with different radiation doses (Vlad et al. 2008), whereas the SS increased in AML cell samples treated with chemotherapy (Kolios et al. 2002; Taggart et al. 2007). The SS decreased for FaDu and Hep-2 cell samples, consistent with an increase in the cellular size after radiotherapy (Vlad et al. 2008). The SS computed from C666-1 cell samples slightly decreased after exposure to radiotherapy from 0.71 ± 0.06 dB/MHz to 0.66 ± 0.14 dB/MHz, consistent with an increase in the cellular size (Table 3).

Table 2. The UIB and cellular size measurements for AML cell samples

Cell type	UIB (dB) ± SE	Cell size (μm) ± variance
AML-viable	−55.4 ± 0.3	10.3 ± 2.3
AML 2 Gy	−51.6 ± 0.6	10.4 ± 4.5
AML 4 Gy	−48.3 ± 0.5	9.2 ± 5.2
AML 8 GY	−49.6 ± 0.6	9.9 ± 4.6
AML-viable	−54.6 ± 0.7	10.6 ± 2.3
AML 12 h	−54.8 ± 1.1	10.6 ± 2.6
AML 24 h	−50.1 ± 1.0	9.6 ± 3.6
AML 48 h	−47.1 ± 0.8	9.6 ± 3.5
AML 72 h	−50.1 ± 1.2	10.1 ± 2.0

Three cell samples were considered for each experimental condition.
SE = standard error.

DISCUSSION

This study explored a mechanism to explain part of the increase in ultrasound backscatter measured from cell samples of four different cell lines that underwent different forms of cell death after exposure to cancer treatment. The changes in UIB are related to a combination of intrinsic scatterer properties, *e.g.*, size, number density and relative acoustic impedance (Lizzi et al. 2003). Changes in each of these properties happen simultaneously during cell death (*i.e.*, increase or decrease of cellular and nuclear size, increase of CSV, nuclear condensation and fragmentation), resulting in complex histological features from which it is difficult to identify the relative contribution of each type of cellular change to ultrasound scattering. This paper focuses on understanding the contribution of changes in cellular size, specifically CSV, to ultrasound backscatter. Ultrasound backscatter increased in cell samples and tissues after different modalities of cell death (Czarnota et al. 1997, 1999; Kolios et al. 2002; Taggart et al. 2007; Vlad et al. 2005; Vlad et al. 2008, 2009); therefore, it is an important parameter to consider in noninvasive detection of cell death using ultrasound methods.

Changes in cellular size, particularly in the CSV, contributed significantly to the UIB increases, as indicated

Table 3. The UIB, DNA content and cellular size measurements for Fadu, Hep-2 and C666-1 cell samples

Cell type	UIB (dB) ± SE	G2M/polyploid (%) (mitotic arrest/ catastrophe)	Cell size (μm) ± variance
FaDu-viable	−50.5 ± 0.7	18.5/1.2	16.6 ± 7.5
FaDu 8 Gy	−46.3 ± 0.8	32.8/9.5	19.9 ± 19.1
Hep2-viable	−52.3 ± 0.4	22.1/1.6	17.4 ± 5.4
Hep2 8 Gy	−45.9 ± 0.6	37.2/12.0	18.0 ± 14.1
C666-1–viable	−45.7 ±1.2	29.3/3.8	13.0 ± 26.0
C666-1 8 Gy	−45.9 ± 0.6	44.7/5.7	14.7 ± 33.3

Three cell samples were considered for each experimental condition.
SE = standard error.

by simulation results (Fig. 3). The increase in CSV had a stronger influence over the increase in UIB for particles with smaller sizes, *e.g.*, 10–15 μm *versus* large particle sizes (*e.g.*, 17 to 20 μm). This indicates that the measured UIB increases depend on choosing an appropriate frequency bandwidth for data collection and analysis in report to what is known about the microstructure of the investigated sample, *e.g.*, cellular and/or nuclear size. The importance of adjusting the ultrasound frequency bandwidth to what is known about the structure of the analyzed sample has also been emphasized by other investigators (Insana et al. 1990; Oelze and Zachary 2006), *e.g.*, the most precise estimates of the scatterer size can be made when ka $\sim$1. This could explain why no increase in UIB was measured between C666-1 viable samples with an initial large CSV (13 $\pm$ 26 μm) and C666-1–treated cell samples, with a further increase of CSV (14.7 $\pm$ 33 μm). Experimental studies at lower frequencies on these cell samples would be relevant. However, it would be very difficult to realize these experiments using lower-frequency transducers because of the requirement imposed on the size of the cell sample. This has to be significantly larger than the cell sample used in this study, requiring tremendous human and technical resources, as well as some modification of cell culture protocols. For example, it takes two weeks to produce enough cells for a cell sample of 8 $\times$ 2 mm (width $\times$ height) (Fig. 1b) as used by the experiments presented in this study.

Interestingly, the tumors grown in mice from C666-1 cell line and treated with radiotherapy exhibited significant changes in the ultrasound parameters, *i.e.*, UIB increased by 6.5 to 8.2 dB (Vlad et al. 2009) in six mouse tumors. This is different from the results obtained in this study, where no significant changes were measured in the ultrasound parameters after treatment of C666-1 cell samples. The comparison of the cellular size distributions from C666-1–viable cell samples and untreated tumors with similar mean of cellular size revealed that CSV was six times larger in cell samples than in tumors. Furthermore, the UIB values computed from the C666-1–viable cell samples were significantly larger (by $\sim$10 dB) than the UIB values measured from untreated C666-1 mouse tumors (Vlad 2009), consistent with the findings of this study. Other investigators (Mamou et al. 2008) have shown that the estimates of the effective scatterer size were biased toward values larger than the mean scatter size for distributions with large variance of particle sizes. Similarly, SS decreased from 0.57 $\pm$ 0.04 to 0.44 $\pm$ 0.07 (Vlad et al. 2008), with increases in CSV and no significant change in mean cellular size (Table 3). These indicate that ultrasound parameters can have different values in cell samples and tumors with similar average cellular size but different CSV. Furthermore, samples with distinct scatterer properties (*e.g.*, $\overline{M}=10\mu m/CSV=8\mu m$ and $\overline{M}=13\mu m/CSV=0\mu m$) could result in similar ultrasound backscatter signatures (Fig. 3). For instance, other studies (Oelze and Zachary 2006) found that scatterer properties estimates were not able to distinguish between some tumor mouse models with different morphological features in histology. Therefore, a good understanding of underlying sample morphology and how this is represented by ultrasound backscatter parameters is necessary to apply the ultrasound techniques effectively for tissue characterization.

The SS can be used to characterize the size of the major scattering structure in tissue as demonstrated previously (Lizzi et al. 1987, 1992, 2003). Previous work from Kolios et al. (2002) demonstrated that the SS increased in AML cell samples that predominantly presented classic features of apoptosis including cell shrinkage and nuclear condensation and fragmentation. In contrast, the SS decreased in cell samples that predominantly underwent mitotic arrest/catastrophe and did not change in the cell samples that underwent a mix of apoptosis and mitotic arrest (Vlad et al. 2008). These changes of SS could be caused by changes of cellular and/or nuclear sizes during different modalities of cell death. Potentially, the SS can be used additionally to UIB as an aid to differentiate the predominant form of cell death in cell samples exposed to different types of therapies.

Our previous experimental investigations have indicated that changes in ultrasound parameters are related to nuclear changes after cell death (Czarnota et al. 1997, 1999; Kolios et al. 2002; Taggart et al. 2007; Vlad et al. 2005; Vlad et al. 2008) because in histology the most obvious changes were observed in the cell nucleus (*e.g.*, nuclear condensation and fragmentation in apoptotic cell death). Other studies (Mamou et al. 2005, 2008; Oelze and Zachary 2006; Oelze and O'Brien 2006) using a spherical Gaussian model to estimate effective scatterer size indicated that scatterer size estimates were close to cellular size. The question of whether the cell or nucleus is the dominant scatterer in cell samples and tumor tissue is important. However, designing the proper experiment to investigate this is difficult because the cell and nucleus are interconnected tightly by mechanical and biochemical process and their size and properties change simultaneously during cell death or other processes (Tannock et al. 2005). For example, qualitative observation on histology and quantitative measurements of cellular size distribution from cell samples exposed to anticancer therapies indicated that both cell and nucleus changed their size after cell death (Vlad et al. 2008). Furthermore, the difference between the cellular and nuclear size is relatively small (*i.e.*, 2 to 5 μm difference in the cellular and nuclear diameters for the cell lines investigated in this study) and the cellular size for the same cell line can vary within a large range,

as indicated in this study, using precise measurements of cellular size. All of these factors increase the difficulty of precisely attributing the changes in ultrasound parameters to either cell or nucleus. Since both cells and nuclei could change their properties during the process of cell death and ultrasound could detect part of these changes it is less relevant for this work whether the cell or nucleus is the dominant scatterer at the frequencies of 10–30 MHz.

A Monte Carlo study on ultrasound backscattering by particles with cell-like properties was used in this study to demonstrate the effect of an increase in CSV on changes in UIB. The results obtained from the simulation revealed that an increase in the variance of particle size in ensembles of randomly positioned particles resulted in an increase in ultrasound backscatter. The differences in the backscattering coefficient between the particle distribution with uniform and heterogeneous size could be enhanced by choosing the appropriate ultrasound bandwidth to increase the sensitivity of cell death detection using ultrasound methods.

The number of iterations required to generate new configurations and consequently to determine converging results of backscattering coefficient (*e.g.*, by taking ensemble average over those configurations) increased exponentially with the number of particles; therefore, the study was limited to 2-D. It would be relevant for future studies to consider 3-D volumes to investigate ultrasound backscattering. Also, the effect of randomization on ultrasound backscattering will be of interest in future studies, because the organization of scatterers can potentially influence the changes in UIB as documented for red blood cells (Cobbold 2006; Mo et al. 1994;) and point scatterers (Hunt et al. 1995, 2002). The long-term goal of this work is to provide an estimate of the percentage of cells responding to the cancer treatment. Therefore, understanding the effect and contribution of each of the cellular changes to ultrasound parameters is important for this type of quantitative assessment. It can be realized by considering multiple factors in the simulation, hence, providing a more comprehensive framework to closely match the experimental conditions.

This study indicated that changes in cellular size, specifically increase of CSV after cell death, had a significant contribution to changes in ultrasound backscattering. This could have important implications for ultrasound characterization of cell death and tissue characterization in general, because CSV increase is common to different forms of cell death (*i.e.*, apoptosis, mitotic arrest/catastrophe, the mix of apoptosis and mitotic arrest/catastrophe). Ultrasound methods can be used to characterize early tumor responses to anticancer therapies in preclinical settings, and potentially in clinical settings (Banihashemi et al. 2008; Vlad et al. 2009). Unlike other imaging modalities for treatment monitoring, *e.g.*, dynamic contrast-enhanced magnetic resonance imaging, single photon emission computed tomography and positron emission tomography, ultrasound does not require injections of contrast agents. The key advantage of the technique is that the image contrast and changes in UIB and SS are caused by changes in physical properties of cells undergoing death and, hence, responding to therapy. Finally, the results suggest that choosing an investigation frequency bandwidth based on what is known about the microstructure of the investigated sample could increase the contrast of ultrasound images and sensitivity of ultrasound parameters, therefore increasing the effectiveness of ultrasound methods to detect cell death.

Acknowledgments—We gratefully thank Dr. Peter Burns and Dr. Liu for valuable discussion, Drs. Deborah Foster and Liu for providing some of the cell lines used in this work and Dr. Nehad Alajez and Anoja Giles for technical support. We also thank "Réseau Québécois de Calcul de Haute performance" (RQCHP) for generous allocation of computer resources. This work was supported by the American Institute of Ultrasound in Medicine's Endowment for Education and Research Grant, Canadian Institutes of Health Research Strategic Training Fellowship Excellence in Radiation Research for the 21st Century; Natural Sciences Engineering Research Council of Canada, Canada Research Chair Program, Canadian Institutes of Health Research, Canadian Foundation of Innovation/Ontario Innovation Trust, Ryerson University; and Sunnybrook Health Sciences Centre, Natural Sciences Engineering Research Council of Canada, Cancer Care Ontario Cancer Imaging Network of Ontario grants.

REFERENCES

Baddour RE, Kolios MC. The fluid and elastic nature of nucleated cells: Implications from the cellular backscatter response. J Acoust Soc Am 2007;121:EL16–EL22.

Bamber JC. Acoustical characteristics of biological media. In: Crocker MJ, (ed). Encyclopedia of acoustics. Toronto: Wiley; 1997.

Banihashemi B, Vlad RM, Giles A, Kolios MC, Czarnota GJ. Ultrasound imaging of apoptosis in tumour response: Novel monitoring of photodynamic therapy effects. Cancer Res 2008;68:8590–8596.

Brindle K. New approaches for imaging tumour responses to treatment. Nat Rev Cancer 2008;82:94–107.

Chin CT. Modelling the behaviour of microbubble contrast agents for diagnostic ultrasound. [Ph.D. thesis] University of Toronto, Canada; 2001.

Cheung ST, Huang DP, Hui AB, Lo KW, Ko CW, Tsang YS, Wong N, Whitney BM, Lee JC. Nasopharyngeal carcinoma cell line (C666-1) consistently harbouring Epstein-Barr virus. Int J Cancer 1999;83: 121–126.

Cobbold RSC. Foundations of biomedical ultrasound. Chapter 5. New York: Oxford University Press; 2006;5–38:46.

Czarnota GJ, Kolios MC, Vaziri H, Benchimol S, Ottensmeyer FP, Sherar MD, Hunt JW. Ultrasonic biomicroscopy of viable, dead and apoptotic cells. Ultrasound Med Biol 1997;23:961–965.

Czarnota GJ, Kolios MC, Abraham J, Portnoy M, Ottensmeyer FP, Hunt JW, Sherar MD. Ultrasound imaging of apoptosis: high-resolution non-invasive monitoring of programmed cell death *in vitro, in situ* and *in vivo*. Br J Cancer 1999;81:520–527.

Darzynkiewicz Z, Juan G, Bedner E. Determining cell cycle stages by flow cytometry. Curr Protoc Cell Biol 2001 May; Chapter 8:Unit 8.4.

Darzynkiewicz Z, Juan G, Li X, Gorczyca W, Murakami T, Traganos F. Cytometry in cell necrobiology: Analysis of apoptosis and accidental cell death (necrosis). Cytometry 1997;27:1–20.

Feleppa EJ, Kalisz A, Melgar S, Lizzi FL, Tian L, Rosado AL, Shao MC, Fair WR, Yu W, Cookson MS, Reuter VE, Heston WDW. Typing of prostate tissue by ultrasonic spectrum analysis. IEEE Trans Ultrason Ferroelectr Freq Control 1996;43:609–619.

Feleppa EJ, Ennis RD, Schiff PB, Wuu CS, Kalisz A, Ketterling J, Urban S, Liu T, Fair WR, Porter CR, Gillespie JR. Spectrum-analysis and neural networks for imaging to detect and treat prostate cancer. Ultrason Imaging 2001;23:135–146.

Feleppa EJ, Porter CR, Ketterling J, Lee P, Dasgupta S, Urban S, Kalisz A. Recent developments in tissue-type imaging (TTI) for planning and monitoring treatment of prostate cancer. Ultrason Imaging 2004;26:163–172.

Hinrichsen EL, Feder J, Jossang T. Random packing of disks in two dimensions. Phys Rev A 1990;41:4199–4209.

Hunt JW, Worthington AE, Kerr AT. The subtleties of ultrasound images of an ensemble of cells: Simulation from regular and more random distributions of scatterers. Ultrasound Med Biol 1995;21:329–341.

Hunt JW, Worthington AE, Xuan A, Kolios MC, Czarnota GJ, Sherar MD. A model based upon pseudo regular spacing of cells combined with the randomisation of the nuclei can explain the significant changes in high-frequency ultrasound signals during apoptosis. Ultrasound Med Biol 2002;28:217–226.

Insana MF, Wagner RF, Brown DG, Hall TJ. Describing small-scale structure in random media using pulse-echo ultrasound. J Acoust Soc Am 1990;87:179–192.

Insana MF, Hall TJ, Wood JG, Yan ZY. Renal ultrasound using parametric imaging techniques to detect changes in microstructure and function. Invest Radiol 1993;28:720–725.

Kolios MC, Czarnota GJ, Lee M, Hunt JW, Sherar MD. Ultrasonic spectral parameter characterization of apoptosis. Ultrasound Med Biol 2002;28:589–597.

Kolios MC, Taggart L, Baddour RE, Foster FS, Hunt JW, Czarnota GJ, Sherar MD. An investigation of backscatter power spectra from cells, cell pellets and microspheres. IEEE Ultrason Symp 2003;1:752–757.

Li JH, Chia M, Shi W, Ngo D, Strathdee CA, Huang D, Klamut H, Liu FF. Tumor-targeted gene therapy for nasopharyngeal carcinoma. Cancer Res 2002;62:171–178.

Lizzi FL, Ostromogilsky M, Feleppa EJ, Rorke MC, Yaremko MM. Relationship of ultrasonic spectral parameters to features of tissue microstructure. IEEE Trans Ultrason Ferroelectr Freq Control 1987;34:319–329.

Lizzi FL, King DL, Rorke MC, Hui J, Ostromogilsky M, Yaremko MM, Feleppa EJ, Wai P. Comparison of theoretical scattering results and ultrasonic data from clinical liver examinations. Ultrasound Med Biol 1988;14:377–385.

Lizzi FL, Astor M, Liu T, Deng C, Coleman DJ, Silverman RH. Ultrasonic spectrum analysis for tissue assays and therapy evaluation. Int J Imaging Sys Technol 1997a;8:3–10.

Lizzi FL. Ultrasonic scatterer-property images of the eye and prostate. Proc IEEE Ultrason Symp 1997b;2:1109–1118.

Lizzi FL, Astor M, Feleppa EJ, Shao M, Kalisz A. Statistical framework for ultrasonic spectral parameter imaging. Ultrasound Med Biol 1997c;23:1371–1382.

Lizzi FL, Feleppa EJ, Kaisar AS, Deng CX. Ultrasonic spectrum analysis for tissue evaluation. Pattern Recognit Lett 2003;24:637–658.

Mamou J, Oelze ML, O'Brien WD Jr, Zachary JF. Identifying ultrasonic scattering sites from three-dimensional impedance maps. J Acoust Soc Am 2005;117:413–423.

Mamou J, Oelze ML, O'Brien JWD, Zachary JF. Extended three-dimensional impedance map methods for identifying ultrasonic scattering sites. J Acoust Soc Am 2008;123:1195–1208.

Metropolis N, Rosenbluth AW, Rosenbluth MN, Teller AH, Teller E. Equation of state calculation by fast computing machines. J Chem Phys 1953;21:1087–1092.

Mo LYL, Kuo I, Shung KK, Ceresne L, Cobbold RSC. Ultrasound scattering from blood with hematocrits up to 100%. IEEE Trans Biomed Eng 1994;41:91–95.

Morse M, Ingard K. Theoretical acoustics. The scattering of sound. Chapter 8. New Jersey: Princeton University Press; 1968. pp. 400–441.

Oelze ML, O'Brien WD Jr. Application of three scattering models to characterization of solid tumors in mice. Ultrason Imaging 2006; 28:83–96.

Oelze ML, O'Brien WD Jr, Blue JP, Zachary JF. Differentiation and characterization of rat mammary fibroadenomas and 4T1 mouse carcinomas using quantitative ultrasound imaging. IEEE Trans Med Imaging 2004;23:764–771.

Oelze ML, Zachary JF. Examination of cancer in mouse models using high-frequency quantitative ultrasound. Ultrasound Med Biol 2006; 32:1639–1648.

Pozarowski P, Grabarek J, Darzynkiewicz Z. Flow cytometry of apoptosis. Curr Protoc Cytom 2003;7:1–23.

Saha RK, Cloutier G. Monte Carlo study on ultrasound backscattering by three dimensional distributions of red blood cells. Phys Rev 2008;78: 061919:1–9.

Savery D, Cloutier G. Effect of red cell clustering and anisotropy on ultrasound blood backscatter: A Monte-Carlo study. IEEE Trans Ultrason Ferroelectr Freq Control 2005;52:94–103.

Shung KK, Thieme GA. Ultrasonic scattering in biological tissues. Boca Raton (FL): CRC Press; 1993. pp. 53–124.

Silverman RH, Folberg R, Rondeau MJ, Boldt HC, Lloyd HO, Chen X, Lizzi FL, Weingeist TA, Coleman DJ. Spectral parameter imaging for detection of prognostically significant histologic features in uveal melanoma. Ultrasound Med Biol 2003;29:951–959.

Taggart LR, Baddour RE, Giles A, Czarnota GJ, Kolios MC. Ultrasonic characterization of whole cells and isolated nuclei. Ultrasound Med Biol 2007;33:389–401.

Tannock IF, Hill RP, Bristow RG, Harrington L. The basic science of oncology. New York: McGraw-Hill; 2005.

Tunis AS, Czarnota GJ, Giles A, Sherar MD, Hunt JW, Kolios MC. Monitoring structural changes in cells with high-frequency ultrasound signal statistics. Ultrasound Med Biol 2005;31:1041–1049.

Twersky V. Acoustic bulk parameters in distributions of pair-correlated scatterers. J Acoust Soc Am 1978;64:1710–1719.

Vlad RM, Alajez NM, Giles A, Kolios MC, Czarnota GJ. Quantitative ultrasound characterization of cancer radiotherapy effects in vitro. Int J Radiat Oncol Biol Phys 2008;72:1236–1243.

Vlad RM, Czarnota GJ, Giles A, Sherar MD, Hunt JW, Kolios MC. High-frequency ultrasound for monitoring changes in liver tissue during preservation. Phys Med Biol 2005;50:197–213.

Vlad RM, Brand S, Giles A, Kolios MC, Czarnota GJ. Quantitative ultrasound assessing tumor responses to radiotherapy in cancer mouse models. Clin Cancer Res 2009;15:2067–2075.

Vlad RM. Quantitative ultrasound characterization of responses to radiotherapy *in vitro* and in vivo. [Ph.D. thesis] University of Toronto; 2009.

Wang C, Koistinen P, Yang GS, Williams DE, Lyman SD, Minden MD, McCulloch EA. Mast cell growth factor, a ligand for the receptor encoded by c-kit, affects the growth in culture of the blast cells of acute myeloblastic leukemia. Leukemia 1991;5:493–499.

Yang M, Krueger TM, Miller JG, Holland MR. Characterization of anisotropic myocardial backscatter using spectral slope, intercept and midband fit parameters. Ultrason Imaging 2007;29: 122–134.